Journal of Materials Chemistry A

Bioinspired Polydopamine Supported on Oxygen-Functionalized Carbon Cloth as a High-Performance 1.2 V Aqueous Symmetric Metal-Free Supercapacitor

Journal:	*Journal of Materials Chemistry A*
Manuscript ID	TA-ART-12-2020-012624.R1
Article Type:	Paper
Date Submitted by the Author:	08-Feb-2021
Complete List of Authors:	Moloudi, Masumeh; Tarbiat Modares University Faculty of Basic Sciences, Chemistry Rahmanifar, Mohammad Safi; Shahed University, bFaculty of Basic Science Noori, Abolhassan; Tarbiat Modares University Faculty of Basic Sciences, Chemistry Chang, xueying; UCLA, Chemistry and Biochemistry Kaner, Richard; University of California Los Angeles, Chemistry and Biochemistry Mousavi, Mir; Tarbiat Modares University Faculty of Basic Sciences, Chemistry; University of California Los Angeles, Chemistry and Biochemistry

ARTICLE

Bioinspired Polydopamine Supported on Oxygen-Functionalized Carbon Cloth as a High-Performance 1.2 V Aqueous Symmetric Metal-Free Supercapacitor

Received 00th January 20xx,
Accepted 00th January 20xx

DOI: 10.1039/x0xx00000x

Masumeh Moloudi, [a] Mohammad S. Rahmanifar, [b] Abolhassan Noori, [a] Xueying Chang, [c] Richard B. Kaner *[c] and Mir F. Mousavi *[a]

The ongoing surge in demand for sustainable energy technologies with little to no environmental impacts calls for the exploration of advanced energy storage materials. Inspiration from nature is undoubtedly a promising approach to comply with environmental legislations. Herein, we describe a facile and green electrosynthesis approach to fabricate a polydopamine (PDA) nanofilm supported on oxygen-functionalized carbon cloth (FCC). The surface functionalization of carbon cloth facilitates the PDA nanofilm adhesion and endows the as-prepared PDA-FCC electrode with excellent flexibility, good electrical conductance (22.6 mS), and outstanding wettability to the aqueous electrolyte. Owing to these merits, the PDA-FCC electrode delivers a favorable capacitance of 626 F g^{-1} at 1.0 A g^{-1} (617 mF cm^{-2} at 2.2 mA cm^{-2}, and 1296 mF cm^{-3} at 5.3 mA cm^{-3}), in which the catechol, amine, and imine moieties of PDA are responsible for its excellent pseudocapacitive behavior. The symmetric all-solid-state flexible PDA-FCC||PDA-FCC device covers almost the entire thermodynamic stability window of aqueous electrolytes (1.2 V), delivers a high specific energy of 11.7 W h kg^{-1}, superb specific power of up to 6.4 kW kg^{-1}, and excellent flexibility along with outstanding cycling stability (81% retention of the initial capacitance after 10,000 cycles). These performance characteristics are in part due to the binder-free PDA biopolymer film that adopts the inherent texture of the carbon cloth, enabling the pores to play the role of temporary ion-buffering reservoirs that facilitate effective mass transport. This new approach to fabricate electrodes from green sources is considered an important step toward environmentally-benign energy storage technologies.

Introduction

The growing global demand for energy to meet the requirements of modern societies is exerting ever-increasing pressure on the environment. One of the most appealing approaches to alleviate these concerns is to develop energy storage technologies that, aside from providing high energy/high power, are more affordable, reliable, sustainable, and environmentally friendly than the existing energy storage systems.[1-3] Progress so far has not, however, been satisfactory to match these expectations. On the other hand, energy access matters more than ever during the COVID-19 pandemic, as energy is key to health care services. COVID-19 will deliberately influence the generation, transmission, and delivery of sustainable energy, as flows of finance and technology rely on a highly interconnected global energy system that hardly seems practicable.[4] Thus, the future of renewable energy sources for electrification of communities, especially islands and remote off-grid areas, looks very bright. In these cases, electrochemical energy storage systems coupled with renewable power generation can help significantly to smooth the load profile and balance the mismatch between supply and demand.[5] Electrochemical capacitors are among the most prominent of these energy storage technologies.

The choice of supercapacitive electrode active materials has been limited mostly to carbon-based materials for electrical double layer capacitors (EDLC),[6-14] as well as transition metal redox species,[15-21] conducting polymers[22-29] and very recently metal-organic frameworks (MOFs),[30-33] layered double hydroxides (LDHs),[34-37] and MXenes[10, 29, 38-40] as redox capacitor materials. To further enhance the supercapacitive performance of the systems beyond EDLCs, our research group and others have developed strategies to fabricate organic redox species-conjugated carbonaceous materials via an intriguing supramolecular non-covalent surface functionalization approach.[41-42] This offers the added benefits of being environmentally benign, cost-effective, remarkably easy to prepare, and metal-free.

Nature is a rich resource that provides a vast wealth of inspirations for scientific discoveries.[43] Bioinspired all-carbon-based materials are a new emerging class of advanced materials

[a] Department of Chemistry, Faculty of Basic Sciences, Tarbiat Modares University, Tehran, P.O. Box 14115-175, Iran, E-mail: mousavim@modares.ac.ir.
[b] Faculty of Basic Sciences, Shahed University, Tehran 3319118-651, Iran.
[c] Department of Chemistry and Biochemistry, Department of Materials Science and Engineering, and California NanoSystems Institute, University of California, Los Angeles (UCLA), CA 90095, USA, E-mail: kaner@chem.ucla.edu.

Electronic Supplementary Information (ESI) available: [Functionalization of carbon cloth and polydopamine synthesis optimization, characterization of the samples, electrochemical studies in 3E and 2E cell setups, comparison of the electrochemical performance of the PDA-FCC electrode and the flexible solid-state PDA-FCC||PDA-FCC device with other studies reported in the literature, and the calculation formula]. See DOI: 10.1039/x0xx00000x

for electrochemical energy storage applications in order to protect sustainable living on our planet.[44] For instance, inspired by mosses grown on rocks in nature, Zhang *et al.* anchored porous carbon nanosheets on bulk carbon backbones and achieved a specific capacitance of 205 F g^{-1} at 0.2 A g^{-1}.[45] In another study, Lian *et al.* dissolved konjac glucomannan, as a natural water-soluble polymer, into an L-cysteine solution and carbonized the mixture in ammonia to prepare a microporous nitrogen-containing carbon that delivered a specific capacitance of 351.7 F g^{-1} at 1.0 A g^{-1}.[46] Inspired by the interfacial interaction design of natural nacre, Wu *et al.* reported a strategy to assemble halloysite-polyaniline-graphene oxide nanocomposite films *via* noncovalent (π-π conjugation, H-bonding, and electrostatic) interactions, which displayed a specific capacitance of 291.2 F g^{-1} at 0.5 A g^{-1}.[47] In another case, Huang *et al*. applied two-level interlocking structures between the electrode active materials and the current collector. They inspired the first interlocking structure by a gecko's feet and the second one by a tree's roots in rock cracks. They developed a flexible micro-supercapacitor with an areal capacitance of 76.6 mF cm^{-2} at 6.25 mA cm^{-2}.[48] Peng *et al.* used Moringa oleifera leaves (heated in an oven at different temperatures from 700 to 900 °C) as the precursor to prepare highly crumpled porous carbons, and achieved a maximum specific capacitance of 260 F g^{-1} at 1.0 A g^{-1}.[49] In another study, Geng *et al*. inspired by the prey-trapping of Venus flytraps fabricated a hierarchical graphene cage that captures lignin to prevent its dissolution, while serving as a three-dimensional electron transport pathway. The designed material displayed a specific capacitance of 211 F g^{-1} at 1.0 A g^{-1}.[50] Aside from these few examples of all-carbon supercapacitors, there are a vast variety of bioinspired supercapacitor chemistries and designs with a wide range of behaviors.[51-53] Invertebrate mussels can strongly adhere to diverse surfaces with high binding strength. It has been reported that 3,4-dihydroxy-L-phenylalanine (DOPA) and lysine-enriched proteins play the major role at the plaque-substrate interface, thus are the key basis of this extraordinary adhesion to virtually all types of surfaces.[54] Hypothesizing that the co-existence of catechol (DOPA) and amine (lysine) functionalities play the central role for adhesion of the mussels to different materials, Messersmith and co-workers identified that dopamine, with a molecular structure containing both catechol and amine moieties, can mimic mussel's adhesion properties.[55-56] Since its advent as a smart coating material in 2007, and because of its outstanding features including adhesive capability, componential tunability, structural complexity and self-healing ability, polydopamine (PDA) has widely been implemented in research and for practical uses, including batteries and supercapacitors.[57-60]

In a bioinspired approach of designing all-carbon electrode active materials for supercapacitive energy storage, herein, we deposited polydopamine onto an oxygen-functionalized carbon cloth (FCC) substrate *via* two very fast, facile, and one-pot electrodeposition methods for the first time. We utilized both constant and pulsed potential techniques and investigated the influence of the electrosynthesis parameters on the characteristics of the PDA film. Polydopamine displays many striking properties as a pseudocapacitive material that lies in its chemical structure that contains catechol, amine, and imine functionalities. *Via* this intriguing surface functionalization approach, we fabricated a binder-free and flexible PDA-FCC electrode that exhibits a high specific capacitance of 626 F g^{-1} at a discharge specific current of 1.0 A g^{-1}. The all-solid-state flexible symmetric PDA-FCC||PDA-FCC supercapacitor displays an extended operating potential window of 1.2 V in a polyvinyl alcohol (PVA)-in-H_2SO_4 gel electrolyte, and exhibits a high specific energy of 11.7 W h kg^{-1} and an excellent specific power of 6.4 kW kg^{-1} along with 81% capacitance retention after 10,000 charge-discharge cycles. This work provides a promising design direction towards the development of more sustainable energy storage devices.

Experimental Section

Materials

Carbon cloth (CC, AvCarb G100, thickness: 0.3 mm) was purchased from FUELCELL store, Texas, USA. The dopamine hydrochloride salt was obtained from Merck, Germany. All other analytical-grade chemicals were purchased from Sigma-Aldrich (USA) or Merck (Germany), and used without further purification.

Apparatus

The morphological and structural characterizations of the electrode active materials were carried out by field-emission scanning electron microscopy (FE-SEM, Philips). Elemental analysis of the samples was obtained using an energy dispersive X-ray spectrometer (EDS, as an attachment to an SEM instrument). The crystallographic characteristics of the FCC and PDA electrodes were recorded using a powder X-ray diffractometer (XRD, Philips X'pert diffractometer with CuK_α radiation (λ = 1.5406 Å) generated at 40 kV and 30 mA with a step size of 0.04° s^{-1}). Raman spectra were collected using an Almega Thermo Nicolet Dispersive Raman Spectrometer. Fourier transform infrared (FT-IR) spectra were obtained from a NICOLET FT-IR 100 spectrometer using KBr pellets. Surface elemental composition and the chemical states of different elements were obtained using X-ray photoelectron spectroscopy (XPS, a Kratos Axis Ultra DLD spectrometer with a monochromatic Al K_α X-ray source (λ = 1486.6 eV)). Specific surface area, pore volume and pore width of the nanostructures were analyzed using BET and BJH procedures by an ASAP 2020 (Micromeritics, USA) instrument.

All electrochemical experiments were performed using a BioLogic SP-300 potentiostat/galvanostat (BioLogic, France) controlled *via* EC-Lab v11.01 software. In all the three-electrode studies, we used a double junction Ag/AgCl in 3.0 M KCl reference electrode and a platinum plate counter electrode, in an aqueous 1.0 M H_2SO_4 solution electrolyte. The cycling stability tests of the PDA-FCC||PDA-FCC symmetric device were recorded using a Solartron 1470A multichannel battery test unit (Solartron Analytical, UK) equipped with Cell Test software (v. 3.5.0). Electrochemical impedance spectroscopy (EIS)

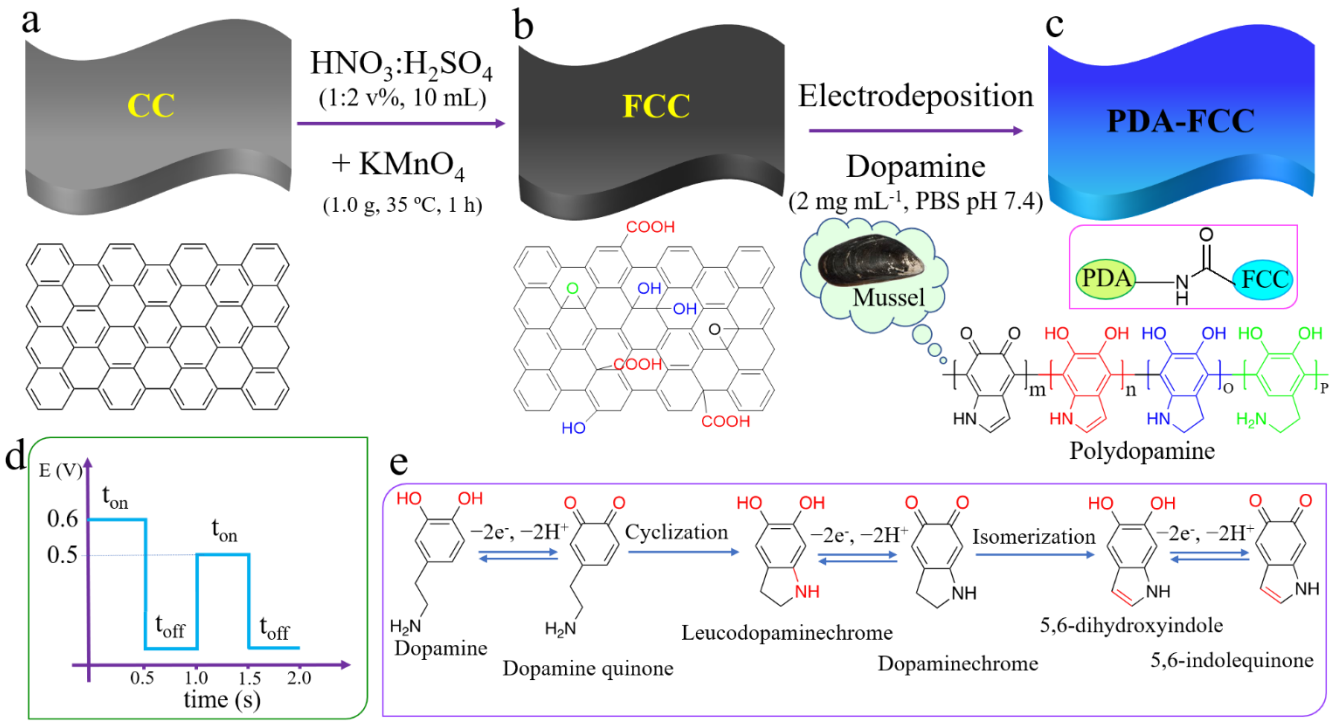

Scheme 1. Schematic illustration of the fabrication process of the PDA-FCC electrode. (a) pristine carbon cloth. (b) Preparation of the functionalized carbon cloth *via* a chemical treatment process using a $KMnO_4$ incorporated mixed HNO_3:H_2SO_4 (1:2, v/v) acidic solution. (c) Electrodeposition of the Mussel-inspired polydopamine film onto the functionalized carbon cloth (FCC) substrate. Covalent conjugation of PDA onto the FCC *via* amide bond formation, as one of the possible conjugation mechanisms, as well as the possible structure of the Mussel-inspired polydopamine film are also presented. (d) A typical pulsed potential waveform for the electrodeposition of dopamine onto functionalized carbon cloth substrate. (e) The possible electrochemical oxidation mechanism of dopamine and formation of the polydopamine film via the formation of dopamine quinone, leucodopaminechrome, dopaminechrome, 5,6-dihydroxyindole, and 5,6-indolequinone intermediates.[2]

measurements were carried out by sweeping the ripple frequency from 100 kHz to 10 mHz and the experimental data were fit using Z-fit in EC-Lab software.

Procedure

Carbon Cloth Functionalization

Functionalization of the pristine carbon cloth (CC) proceeded according to the methods reported previously with a slight modification.[61-64] For chemical functionalization of the carbon cloth substrate, we first cleaned the pieces (1.0 cm × 1.0 cm) by sonication in a 1:1 acetone-ethanol mixture for 30 min. Then, we dipped the pieces of CC in a concentrated HNO_3:H_2SO_4 (1:2, v/v) solution (10 mL) for 5 min. After that, $KMnO_4$ (1.0 g), as an oxidizing agent, was immediately added into the solution and stirred at 35 °C for 1 h. Next, the solution was diluted by adding 100 mL of distilled water and kept stirring for 3 h. In the next step, H_2O_2 solution (30%), that reacts with $KMnO_4$ to produce MnO_2 and O_2, was added until the gas evolution stopped (Fig. S1a). Finally, the functionalized carbon cloth (FCC) pieces were thoroughly rinsed with distilled water, followed by drying in an oven at 60 °C for 3 h. Chemical functionalization of the carbon cloth in a mixed acid solution containing an oxidizing agent introduces oxygen-containing surface functional groups as outlined in Scheme 1a,b.

Deposition of Polydopamine onto Functionalized Carbon Cloth

The synthesis solution is a phosphate buffer solution (PBS, 0.1 M, pH 7.4) containing dopamine (2.0 mg mL^{-1}). We electrodeposited polydopamine onto the FCC *via* two different methods; constant potential (CP) and pulse potential techniques. The constant potential method involves applying a nucleation potential of 0.6 V (vs. Ag/AgCl) for a short time (20 s) followed by a growth potential of 0.5 V for 600 s. The growth time is optimized so that the deposited PDA was ~1.0 mg cm^{-2}. *Via* the pulse electrodeposition method (Scheme 1c,d), the potential of the working electrode is stepped from a rest potential to 0.6 V for 0.5 s, where the nucleation takes place. After 0.5 s rest, the potential is stepped to 0.5 V for the optimized time of 0.5 s (Fig. S2), a potential where nucleation rate is slow, instead, the previously formed nuclei grow. This electrodeposition method allows fine control over the particle size and morphology of the electro-synthesized PDA film. The number of consecutive nucleation and growth pulses are controlled so that the electrodeposited PDA film is ~1.0 mg cm^{-2}. After electrodeposition, the obtained PDA-FCC electrode was washed with distilled water and dried at 60 °C for 3 h. Electrosynthesis of the polydopamine film that likely involves oxidation of dopamine to dopamine–quinone, its intramolecular cyclization and formation of leucodopaminechrome, oxidation of leucodopaminechrome to dopaminechrome, formation of 5,6-dihydroxyindole and its oxidation to 5,6-indolequinone are outlined in Scheme 1e.[65]

Results and Discussion

Design Considerations

Capacitive behavior of the carbon-based materials can be divided into two subclasses: (i) electrical double layer capacitors (EDLCs), and (ii) pseudocapacitors.[66] Apart from a high specific surface area and the extensively developed porosity, where the ions are adsorbed to form an electrical double layer, surface functionalization of the carbonaceous materials, to incorporate Faradaic redox reaction sites, is an efficient approach for tailoring their energy storage performance.[67] Surface modification *via* molecular design is a promising approach to confer new functionalities into existing materials, a feature that is particularly important in the field of energy storage. On account of its similar molecular structure with DOPA and tyrosine amino acid in mussel adhesive proteins, PDA can strongly adhere to a variety of substrates.[54, 56-57] In addition, PDA exhibits a promising prospect for energy storage as a nitrogen-containing carbon matrix. The presence of catechol and amine functional groups that act as active sites for Faradaic redox reactions along with excellent biocompatibility, easy preparation, controllable thickness, self-healability,[68-69] and an outstanding wettability endow PDA with extraordinary energy storage performance. Functionalized carbon cloth (FCC) was chosen as a substrate owing to its low cost, chemical stability, high electrical conductivity, and mechanical flexibility. This new type of energy storage material is well suited for high power metal-free green energy storage applications.

Physico-chemical Characterizations

We investigated the surface morphology of the pristine CC as well as the FCC and PDA-FCC electrodes using a field-emission scanning electron microscope (FE-SEM). FE-SEM image of the pristine CC is composed of interlaced carbon fibers with a smooth surface (Fig. 1a). After functionalization, the interlaced structure of the carbon fibers has not been destroyed, instead numerous grooves and wrinkles are formed on the FCC surface which impart a relatively coarse surface for better polydopamine hosting (Fig. 1b). The FE-SEM images of the PDA-FCC electrode, synthesized *via* a constant potential method, show a complete and uniform PDA film electrodeposited onto FCC surface (Fig. 1c). The FE-SEM image also reveals a rather uniform size distribution (~20 nm) with a granular morphology of the polydopamine film. Whereas, the PDA-FCC electrode, synthesized *via* a pulse deposition method, shows a nanowall network that is well-oriented with the c-axis, and perpendicular to the FCC substrate surface (Fig. 1d,e). We analyzed the elements in FCC and PDA-FCC using energy dispersive X-ray spectroscopy (EDS). The EDS spectrum of FCC (Fig. S3) displays the peak of oxygen (besides the peak of carbon) that can be attributed to the oxygen-bearing functional groups induced *via* acidic $KMnO_4$ treatment. The spectrum of PDA-FCC shows an additional strong elemental peak for nitrogen, demonstrating that the FCC is covered entirely by polydopamine. EDS spectral mapping of the PDA-FCC sample shows a homogeneous distribution of N, C, and O elements, demonstrating the atomic-scale and uniform coverage of the polydopamine film on the substrate (Fig. 1f). We also characterized the pristine as well as the modified carbon cloths using Fourier transform infrared (FT-IR) spectroscopy. The FT-IR spectrum of the FCC displays some prominent bands that were not very noticeable in the spectrum of the pristine CC (Fig. 2a). A broad band at ~3400 cm^{-1} in the spectrum of FCC is attributed to the stretching vibration of the hydroxyl groups. The band at 1727 cm^{-1} is ascribed to the presence of carboxylic acid and carbonyl functional moieties on the FCC surface. The peak at 1630 cm^{-1} is associated with the skeletal vibrations of the aromatic rings, and a broad band over 1000-1400 cm^{-1} is attributed to the C-OH and C-O stretching modes. Thus, FT-IR spectroscopy provides strong evidence for successful functionalization of the carbon cloth.[70] In the FT-IR spectrum of the pulse-deposited PDA-FCC, the bands appearing at 3200, 1500 and 1398 cm^{-1} originate from N-H stretching, N-H bending, and C-N stretching vibrations, respectively. The characteristic band of C-N at 1398 cm^{-1} along with the decrease in the intensity of the band at 3400 cm^{-1} is known as demonstrative evidence of covalent conjugation of PDA onto FCC *via* amide bond formation.[71-72]

Raman spectroscopy is often used to characterize carbon-based materials. Raman spectra of the CC, FCC, and pulse-deposited PDA-FCC samples clearly present two well-known bands, the G-band which originates from the sp^2 hybridized carbon and the D-band that arises from the disordered sp^3 hybridized carbon (Fig. 2b). The intensity ratio of the D to G bands (I_D/I_G) can help to estimate structural disorder of the carbon-based materials where a higher ratio indicates more defects on the sample. The value of I_D/I_G for the FCC is higher than that of the pristine CC due to the oxygen-containing functional groups that induce more structural defects.[73] After electro-polymerization of PDA onto the FCC, the I_D/I_G value decreases which can be ascribed to the formation of covalent bonds between functional groups of the FCC and the catechol or amine moieties of PDA that partially compensates for the structural disorder.[71, 74] The slight shift of the D and G bands for the PDA-FCC sample can be ascribed to the conjugation of PDA to the functional groups of the FCC.

We conducted X-ray photoelectron spectroscopy (XPS) to provide further insights into the surface elemental composition of the FCC and PDA-FCC samples (Fig. 2c-e). In addition to the characteristic peak of carbon (C 1s), the survey XPS spectrum of FCC shows the characteristic peaks of oxygen (O 1s) as well, originating from the successful incorporation of the oxygen-bearing functionalities into the FCC. The survey XPS spectrum of the PDA-FCC (Fig. S4) clearly indicates the coexistence of carbon (C 1s), oxygen (O 1s) and nitrogen (N 1s) in the sample (the peak at ~496 eV can be attributed to adsorbed sodium ions, Na KLL auger peak). The results of the XPS study are consistent with the outputs of the Raman, XRD and FT-IR analyses, confirming proper electrodeposition of PDA on the FCC samples. The curve-fitted core level XPS spectrum of the C 1s of FCC shows five different characteristic peaks. The peaks located at 284.8 and 285.1 eV come from the C=C and C–C bonds in the aromatic rings, and the peaks centered at 285.8, 286.9, and 288.7 eV correspond to the C–O (epoxy and alkoxy), C=O, and O–C=O groups, respectively.[63, 71, 75] The small shift observed in

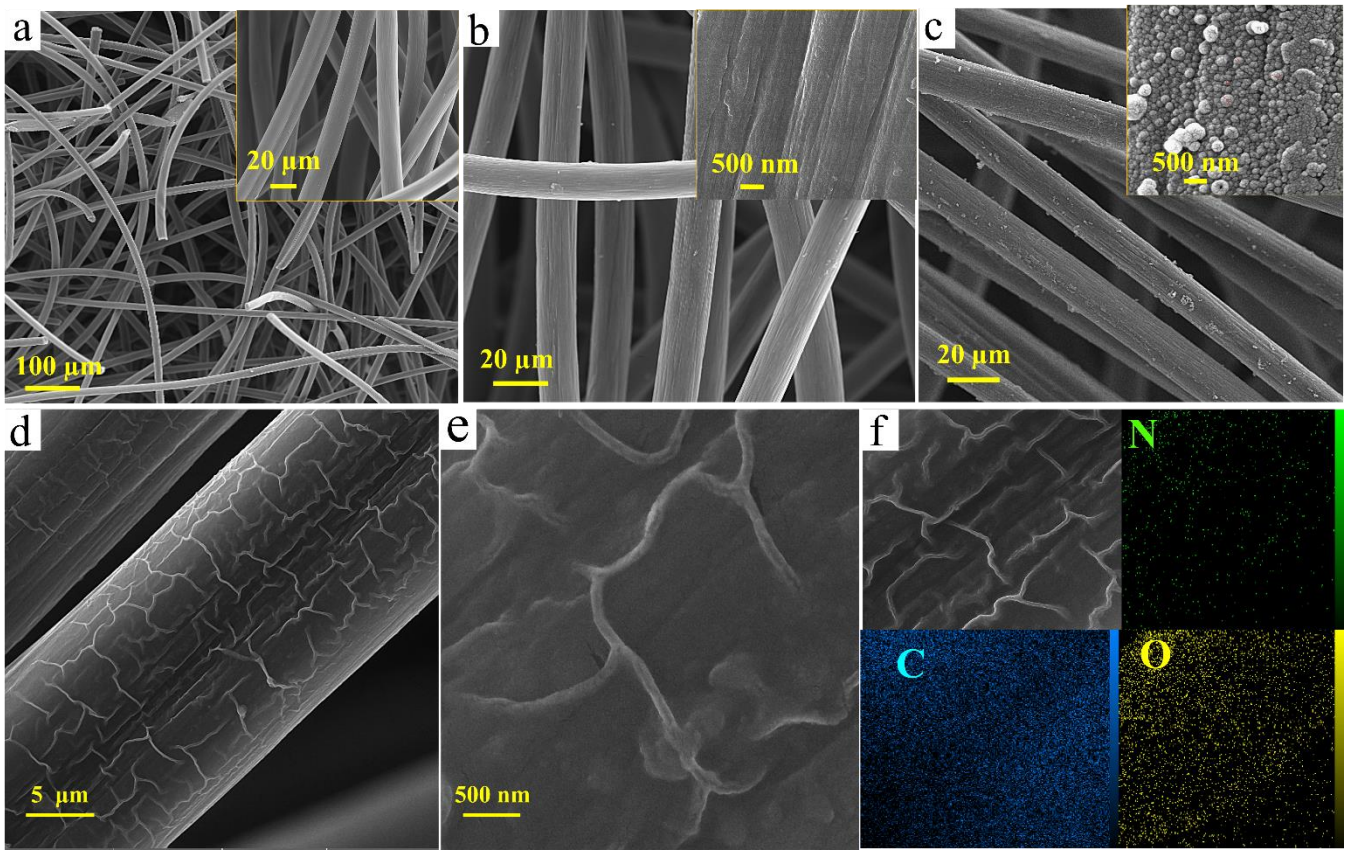

Fig. 1 Morphological characterizations of the CC, FCC and PDA-FCC. FE-SEM images of the (a) carbon cloth (CC), (b) functionalized carbon cloth (FCC), (c) constant potential deposited PDA-FCC, and (d, e) pulse deposited PDA-FCC electrodes. The insets show the images with a higher magnification. (f) Energy dispersive X-ray (EDS) elemental mapping of nitrogen, carbon, and oxygen of the PDA-FCC sample.

the curve-fit core level XPS spectrum of the C 1s of FCC after electro-polymerization of PDA onto the FCC can be ascribed to covalent conjugation of the FCC functional groups to the catechol or amine moieties of PDA. Figure 2d-e display the curve-fit core level XPS spectra of the C 1s and N 1s of the pulse-deposited PDA-FCC. The deconvoluted core-level XPS spectrum of C 1s of PDA-FCC consists of six peaks that are attributed to: aromatic carbon (C=C, 284.0 eV), aliphatic carbon (C-C, 285.0 eV), carbon-nitrogen and epoxy (C–N, C-O-C, 286.1 eV), hydroxyl (C-OH, 287.4 eV), carbonyl (C=O, 289.0 eV), and carboxyl (HO-C=O, 292.5eV) groups. The peak located at 286.1 eV, which is absent in the deconvoluted core-level C 1s spectrum of the FCC, is attributed to the C-N bond and confirms the successful polymerization of PDA onto the FCC. The C–N=C, C–NH and C–NH_2 broad peaks appearing at the binding energies of 397.8, 399.0 and 400.0 eV in the core level N 1s spectrum correspond to the amino nitrogen atoms and heterocyclic nitrogen atoms, respectively. The presence of the primary amine is ascribed to the noncovalent self-assembly of dopamine. Presence of the secondary amine indicates the formation of the heterocyclic ring of indolic moieties in the structure of the polydopamine hetropolymer. [60, 76-77] We also compared the chemical state and surface composition of the nitrogen-containing functional groups (including imine (−N=), pyrrolic (−NH−), and amine (−NH_2) functionalities) of the PDA-FCC electrodes prepared *via* pulse- and CP-deposition methods (Table S2 and Fig. S5). As can be seen, the pyrrolic N moieties are quite prevalent in the pulse-deposited PDA-FCC structure, whereas the imine functionalities dominate in the structure of the CP-deposited PDA-FCC.

We also used X-ray diffraction (XRD) to investigate the effect of the chemical treatment on CC. Fig. S6 displays the XRD patterns of the CC, FCC and FCC-PDA samples. All of the samples show two broad diffraction peaks at 2θ values of 25.5°and 43° which can be attributed to the (002) and (101) planes of the amorphous graphitic CC structure.[64] The lower intensity of the XRD bands of the FCC, compared to that of the CC, demonstrates a lower degree of graphitization of the FCC, due to the presence of some functional groups in its structure.

To investigate the surface area and pore-size distribution that significantly affects specific capacitance and the rate performances of the nanoporous materials,[78-79] N_2 adsorption-desorption measurements of FCC and PDA-FCC electrodes were conducted by Brunauer-Emmett-Teller (BET) and Barrett-Joyner-Halenda (BJH) methods, respectively. As shown in Fig. 2f, according to N_2 adsorption-desorption isotherms, all the samples display type IV isotherms with H1-type hysteresis loops, which indicate the formation of mesoporous structures. Wide pore-size distribution of pulse-deposited PDA-FCC compared to FCC can be extremely beneficial to amplify the kinetics of the reactions to attain

enhanced supercapacitive performances. The wide range of mesopores guarantees

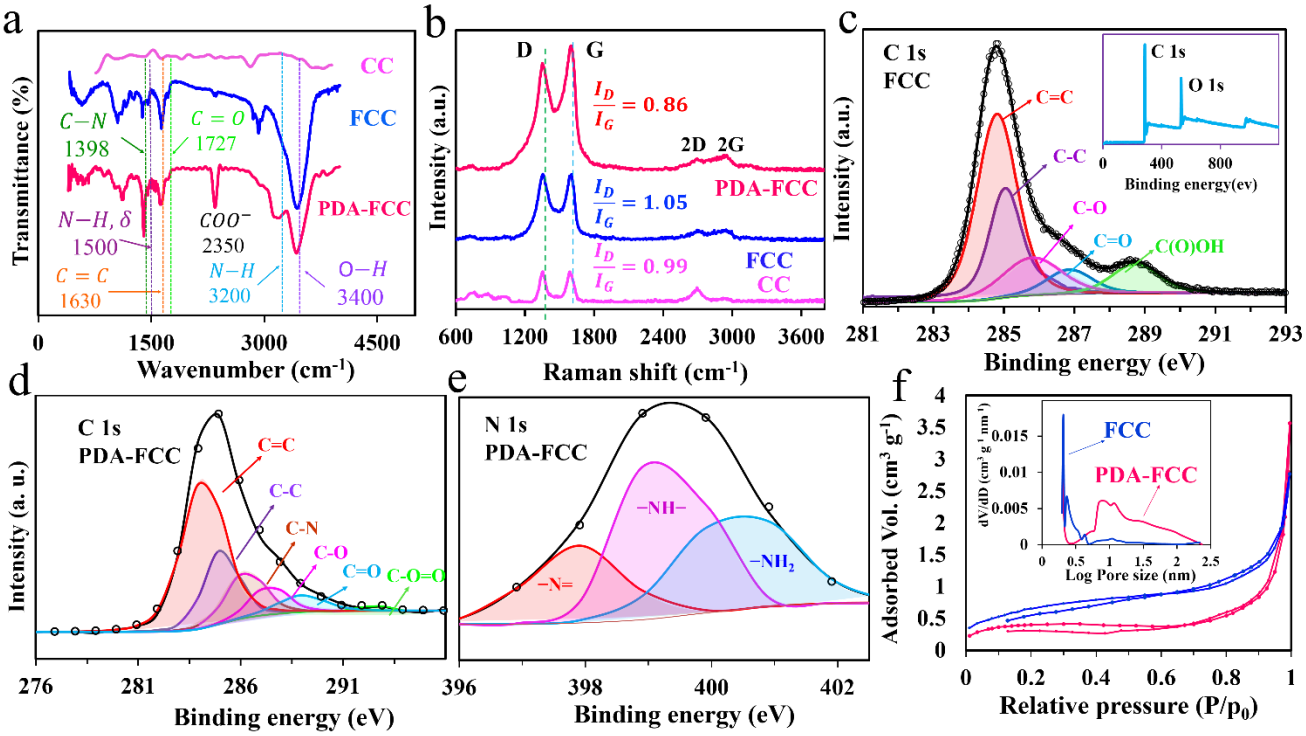

Fig. 2 Structural characterizations of the CC, FCC and pulse-deposited PDA-FCC. (a) FT-IR spectra, and (b) Raman spectra of the CC, FCC, and PDA-FCC electrodes. (c) Deconvoluted core level XPS spectrum of the FCC, C 1s. The inset shows the survey XPS spectrum of the FCC sample. Deconvoluted core level XPS spectra of the PDA-FCC electrode; (d) C 1s, and (e) N 1s. (f) *Nitrogen adsorption–desorption isotherms of FCC (blue) and PDA–FCC (red) electrodes.* The inset shows *BJH pore size distributions of the FCC and PDA–FCC samples.*

abundant electroactive sites for Faradaic reactions, meanwhile providing low-resistance ion transport pathways in the PDA-FCC film.[80–81] The lower surface area of PDA-FCC (8.5 $m^2 g^{-1}$) is due to the occupation of some of the pores with electrodeposited PDA.

Electrochemical Studies in a 3E Cell Setup

We employed a three-electrode cell setup to study supercapacitive performance of the CC, FCC and PDA-FCC electrodes using cyclic voltammetry (CV), galvanostatic charge-discharge (GCD) and electrochemical impedance spectroscopy (EIS) measurements in a 1.0 M H_2SO_4 solution as the electrolyte. Through these studies, we optimized the PDA-FCC electrode for the best supercapacitive performance, investigated the electrochemical performance of the materials, and deconvoluted the contribution from the capacitor-like and battery-like behavior in the total charge. The morphology and thickness of the polydopamine film for supercapacitive energy storage were tailored by the applied deposition technique. Note that for energy storage applications, electrodes are typically prepared by casting the slurry, comprised of the chemically synthesized active material, a conductive additive, and a binder, onto a substrate. The conductive additives and binders, which are required to preserve a firm structure and to provide continuous electron transfer pathways, do not contribute significantly to the energy storage process, and hence, reduce capacitance/energy/power of the system. In contrast, electrodeposition of the active material onto the substrate provides a strongly adhering deposit, the thickness and morphology of which can be easily tuned by manipulating the applied potential or current.

Fig. 3a shows the CV curves of the acidic $KMnO_4$ treated FCC electrode as well as the PDA-FCC electrodes prepared *via* a constant potential method and a pulse potential technique (denoted as CP and pulse, respectively) at a scan rate of 20 mV s^{-1}. CV curves of the pristine CC and the $KMnO_4$-free mixed acid (concentrated (1:2, v/v) HNO_3:H_2SO_4) treated FCC are presented in Fig. S1b. The negligible integrated area of the CC electrode indicates that the pristine substrate has almost no contribution to the capacitive performance of the system. The CV curve of the FCC shows a pseudo-rectangular shape from –0.2 to 1.0 V. The well-defined redox peaks in the CV curve of the FCC can be ascribed to the functional groups (-C=O, -C-OH and -COOH) introduced onto the FCC surface *via* an acidic $KMnO_4$ treatment. These oxygen-containing functional groups not only allow proper chemical conjugation of the polydopamine, but also the remnant functionalities induce a net pseudocapacitance to the system. Compared with the FCC electrode, the CP-deposited PDA-FCC electrode displays a CV curve with a noticeably enhanced area (almost three times as large as the area under

the CV curves of the FCC electrode). The two couples of reversible and stable redox peaks in the CV curves of the PDA-FCC are assigned to the oxidation of dopamine to dopamine quinone, which undergoes an intra-molecular cyclization reaction to yield leucodopaminechrome, and subsequent oxidation of leucodopaminechrome to dopaminechrome

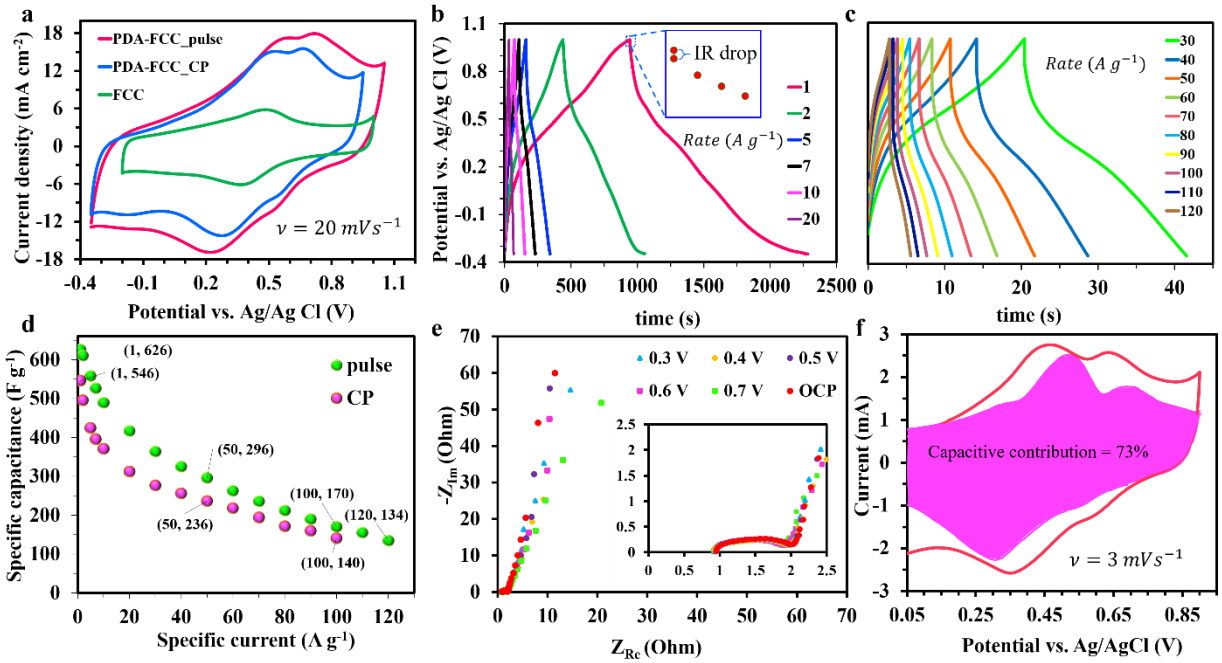

Fig. 3 Investigation of the electrochemical performances of the prepared electrodes in a three-electrode cell setup. (a) CV curves of the FCC as well as the constant potential and pulse deposited PDA-FCC electrodes at a scan rate of 20 mV s^{-1} in an aqueous 1.0 M H_2SO_4 electrolyte. (b, c) GCD profiles of the pulse deposited PDA-FCC electrode at different specific currents ranging from 1 to 120 A g^{-1}. The inset of panel b shows the magnified view of the initial stage of the discharge step, IR drop. (d) Rate capability study; specific capacitances of the constant potential and pulse deposited PDA-FCC electrodes at different specific current values. (e) A series of Nyquist plots measured at various potentials of the CV curve (0.3, 0.4, 0.5, 0.6, 0.7 V and open circuit potential (OCP) over a frequency range from 100 kHz to 10 mHz. The inset shows a magnified high frequency region. (f) Decoupling the contribution of capacitive and battery-like charge storage processes for a PDA-FCC electrode at a scan rate of 3.0 mV s^{-1}.

(Scheme 1e).[74] Note that, despite the fact that polydopamine can be prepared *via* a facile electrodeposition process, the molecular mechanism behind its polymerization has long been the topic of scientific debate due to the complexity of the redox processes as well as the diversity of the reactive intermediates that are formed during dopamine polymerization.[54, 65] It has recently been proposed that both covalent and noncovalent interactions are involved in the polymerization process, and the dopamine species are held together *via* a combination of H-bonding, π-π stacking, and charge transfer interactions. [74] Thus, it is likely that a complex series of reactions take place on the PDA-FCC electrode and the mechanism presented in Scheme 1e is simply the most widely proposed mechanism.

The CP-deposited PDA-FCC electrode exhibits a significantly extended potential window that spans from −0.35 to 0.95 V (0.1 V wider that the FCC electrode) along with a predominant pseudocapacitive nature. The PDA-FCC electrode prepared *via* a pulse deposition method exhibits an even larger CV integrated area (~3 times as large as the FCC electrode) along with a much wider operating potential window that spans from −0.35 to 1.05 V (0.2 V wider that the FCC electrode). The wider operating potential window of the pulse-deposited PDA-FCC electrodes indicates that electro-polymerization of dopamine onto the FCC stabilizes the active material, which is of paramount importance for supercapacitors. Expansion of the operating potential window of the PDA-FCC electrodes, which is a straightforward approach towards enhancing the energy storage performance of supercapacitors, can likely be explained by the hydrogen-bonding capability of the polydopamine moieties and hence the kinetic barriers along the H_2 and O_2 evolution reaction pathways. Stadler and co-workers have (experimentally and theoretically) shown that among the different intermediate oxidation products of dopamine formed during polymerization, just keto-indoleamine hydrogen-bonds possess a low hydrogen binding energy (ΔG_H^*) whereas the other intermediate oxidation products are so far from the summit of the so-called Volcano plot.[82] The better energy storage performance of the pulse deposited PDA film demonstrates that size and morphology play a vital role in defining the energy storage performance of the materials. The obtained values of the areal capacitances (at a scan rate of 20 mV s^{-1}) are 165.0, 470.8, and 535.7 mF cm^{-2} for the FCC, PDA-FCC CP, and PDA-FCC-Pulse, respectively (please see the Supporting Information for the calculation formulas). The enhanced supercapacitive performance of the pulse deposited PDA-FCC electrode can be ascribed to the high surface area, better wettability of the aqueous electrolyte to the polydopamine film (see the supporting information, Fig. S7 and Video S1), and higher conductivity of the PDA-FCC electrodes (discussed later on) compared with the FCC.

Fig. S8 and S9 illustrate typical CV curves of the PDA-FCC electrode at different scan rates ranging from 1 to 200 mV s^{-1} for the CP-deposited and 1 to 300 mV s^{-1} for the pulse-deposited PDA-FCC electrodes, respectively. As can be seen, the CV curves of the PDA-FCC electrode imply excellent capacitive behavior with almost-vertical current switches at potential extremes. This demonstrates a fast charge transport within the PDA-FCC, thanks to the efficient electronic coupling between the polydopamine film and the FCC substrate. Even at a high scan rate of 300 mV s^{-1}, the pulse-deposited PDA-FCC electrode exhibits a couple of broad redox peaks superimposed on a rectangular profile, demonstrating the excellent reversibility of the Faradaic processes and improved pseudocapacitive performance of the PDA-FCC electrode.

We further conducted GCD measurements at various specific currents ranging from 1.0 to 120.0 A g^{-1}, in an extended potential window (1.3 V), to evaluate the capacitive performance of the pulse deposited PDA-FCC electrode (Fig. 3b,c). GCD profiles of the CP deposited PDA-FCC electrode are presented in Fig. S10. GCD profiles display a very low iR drop at the initial stage of the discharge step across all current regimes (Fig. 3b, inset). GCD profiles also display an intermediate region (from 0.3 to 0.6 V) with a mild slope that is assigned to the reversible Faradaic charge-discharge processes taking place on the PDA-FCC electrode (that is in accordance with the CV curves). The CP deposited PDA-FCC electrode exhibits a high specific capacitance of 546 F g^{-1} at a discharge rate of 1.0 A g^{-1} (277 F g^{-1} at 1.0 A g^{-1} based on the total mass of the electrode, i.e. PDA plus FCC) and retains capacitance of 140 F g^{-1} at a high discharge rate of 100.0 A g^{-1} (Fig. 3d). However, the pulse deposited PDA-FCC electrode displays an excellent capacitance of 626 F g^{-1} at a discharge rate of 1.0 A g^{-1} (367 F g^{-1} at 1.0 A g^{-1} based on the total mass of the electrode) and retains capacitances of 170 and 134 F g^{-1} at high discharge rates of 100.0 and 120.0 A g^{-1}, respectively. This demonstrates outstanding supercapacitive performance and excellent high-rate capability of the PDA-FCC electrodes, especially the pulse-deposited one (Fig. 3d). The high-rate capability and low *iR* drops at all discharge rates can be attributed to the efficient interaction of PDA with the FCC. This sustainable behavior in a wide current range originates from the cumulative energy storage performance of the PDA and FCC in the PDA-FCC electrode that benefits from the improved wettability and increased conductivity of the porous PDA-FCC, in which the surface of the electrode active material is easily accessible to the electrolyte ions. The low-cost, ease of synthesis and excellent pseudocapacitive performance of the resulting PDA-FCC electrode is superior to most of the previously reported metal-free supercapacitive materials and comparable to the other pseudocapacitive materials reported in the literature (Table S3).

We conducted EIS studies to obtain further insight into the electrochemical kinetics of the PDA-FCC electrode, which confirmed the trend of CV and GCD studies. Fig. 3e displays the Nyquist plots of the PDA-FCC electrode (over the frequency range from 100 kHz to 10 mHz) at five different potentials as well as the open circuit potential (OCP). A representative voltammogram of the PDA-FCC electrode with the assigned potentials is presented as Fig. S11a. An expanded view of the high-frequency region is presented as an inset to Fig. 3e, and the equivalent circuit fit to the experimental data is displayed in Fig. S11b. The extracted parameters corresponding to the equivalent circuit model are presented in Table S4. The Z_{re}-intercepts of the Nyquist plots after extrapolation of the trend in the high frequencies (which represents the equivalent series resistance, ESR), show very low values with only a slight variation at different electrode potentials (ESR values are in the range from 0.85-0.91 Ω). The low ESR values, which comprises the ionic resistance of the electrolyte and the electronic resistance of the electrode, clearly suggests a high conductivity for the PDA-FCC electrode. Two depressed overlapping semicircles at high and middle-frequency domains, and a near-vertical line at the low-frequency region, can also be seen in the Nyquist plot of the PDA-FCC electrode. The diameter of the high-frequency semicircle (R1) is potential-dependent and slightly decreases upon increasing the applied potential; thus, the value of R1 is attributed to charge transfer resistance.[83-84] The diameter of the semicircle in the middle-frequency region is potential-independent, and thus can be ascribed to the diffusion resistance of the electrolyte within the voids in between the fiber bundles of the FCC.[85-89] The amounts of the Warburg impedance of the PDA-FCC electrode at the pre-peak (0.4 V), peak (0.5 V) and post-peak (0.6 V) potentials are 0.12, 0.79 and 0.15 Ω $s^{-1/2}$, respectively (Table S4). The significantly higher value of the Warburg impedance at peak potential clearly indicates a large contribution from diffusion-controlled redox processes in energy storage performance of the PDA-FCC at the peak potential compared to the other applied potentials. As can be seen in the Bode phase plot (Fig. S11c), the phase angle of the PDA-FCC electrode at low frequencies is −75.4°, which is far from the −90° for ideal capacitors. In addition, a slope of ~−0.78 in the low frequency region of the Bode magnitude plot shows a significant deviation from the −1.0 expected for ideal capacitors. These characteristics imply a combination of capacitive and battery-like behavior of the electrode active material, although the capacitive behavior dominates the mechanism. The RC time constant was calculated as 0.69 s from the Bode phase plot at a phase angle of about −45° (exactly −44.89°) indicating an enhanced ion transport rate in the PDA-FCC electrode.

Based on the power law dependence of the current (i) on the sweep rate (ν) using the equation $i = a\nu^b$, which enables fast determination of the electrode kinetics, a *b*-value of 0.72 was obtained (Fig. S12), demonstrating a behavior in the transition area from a battery-like (b = 0.5) to a supercapacitor-like (b = 1.0) response.[66,90] A critical issue in the study of energy storage materials is the deconvolution of the contribution from capacitive and battery-like processes in the total charge of the electrical energy storage system. Figure 3f shows that the potential profile for the capacitive current (the shaded region) accounts for 73% of the total charge at a sweep rate of 3 mV s^{-1}, demonstrating the fast kinetics and high-rate capability of the system.

Fabrication of a Symmetric PDA-FCC||PDA-FCC Device

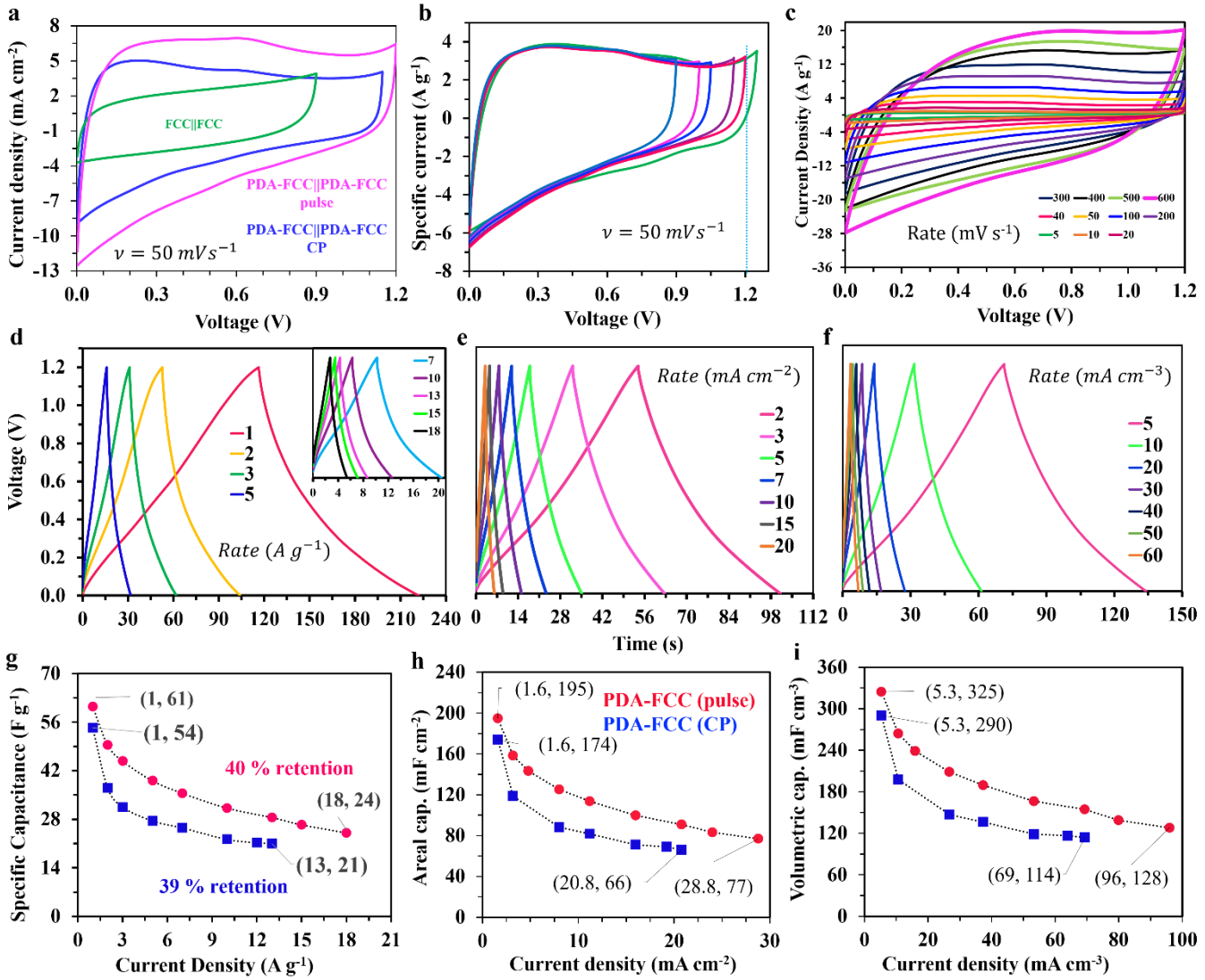

Fig. 4 Electrochemical studies of the symmetric PDA-FCC||PDA-FCC and FCC||FCC devices in a PVA-in-H_2SO_4 gel electrolyte. (a) CV curves of the FCC||FCC device as well as the PDA-FCC||PDA-FCC devices, the materials of which were prepared *via* either a constant potential or a pulsed waveform (v = 50 mV s^{-1}). (b) CV curves of the pulse deposited PDA-FCC||PDA-FCC device at different voltage windows (v = 50 mV s^{-1}). (c) CV curves of the pulse deposited PDA-FCC||PDA-FCC device at various scan rates from 5 to 600 mV s^{-1}. (d-f) GCD profiles of the pulse-deposited PDA-FCC||PDA-FCC device at different specific current values from 1.0–18.0 A g^{-1} (d), areal current densities from 2.0 to 20.0 mA cm^{-2} (e), and volumetric current densities from 5 to 60 mA cm^{-3} (f). (g-i) Rate capability studies of the constant potential (blue squares) and pulse-deposited (red circles) PDA-FCC||PDA-FCC devices at different specific currents (g), areal current densities (h), and volumetric current densities (i).

To assess the suitability of the PDA-FCC electrode as a promising active material for energy storage applications, we fabricated a solid-state symmetric PDA-FCC||PDA-FCC device by PDA-FCC as both the negative and positive electrode. We also fabricated a symmetric FCC||FCC device to form a basis for comparison of our newly developed device. We used a polyvinyl alcohol (PVA)-in-H_2SO_4 (1.0 M) gel electrolyte and stainless steel (SS) grid current collector in both the devices. Figure 4a displays CV curves of the FCC||FCC device, as well as the two PDA-FCC||PDA-FCC devices, the active materials of which are prepared *via* constant potential and pulse deposition techniques, at a scan rate of 50 mV s^{-1}. As can be seen, the FCC||FCC device shows a tilted CV profile with a significant distortion from a rectangular shape at the starting and switching voltages, whereas, the PDA-FCC||PDA-FCC supercapacitors display voltammograms with almost-vertical current switches at voltage extremes. However, the pulse deposited PDA-FCC||PDA-FCC supercapacitor exhibits a significantly higher enclosed area and a wider voltage window than the CP-deposited PDA-FCC||PDA-FCC and FCC||FCC supercapacitors, demonstrating its superior energy storage performance. The obtained values of areal capacitance at a scan rate of 50 mV s^{-1} are 129.3, 74.8 and 43.4 mF cm^{-2} for the pulse-deposited PDA-FCC||PDA-FCC, CP-deposited PDA-FCC||PDA-FCC and FCC||FCC devices, respectively (Fig. 4a). The enhanced pseudocapacitive performance of the PDA-FCC||PDA-FCC devices can be attributed to the rich redox functional groups of the polydopamine and the improved wettability as well as the enhanced conductivity of the PDA-FCC electrode material.

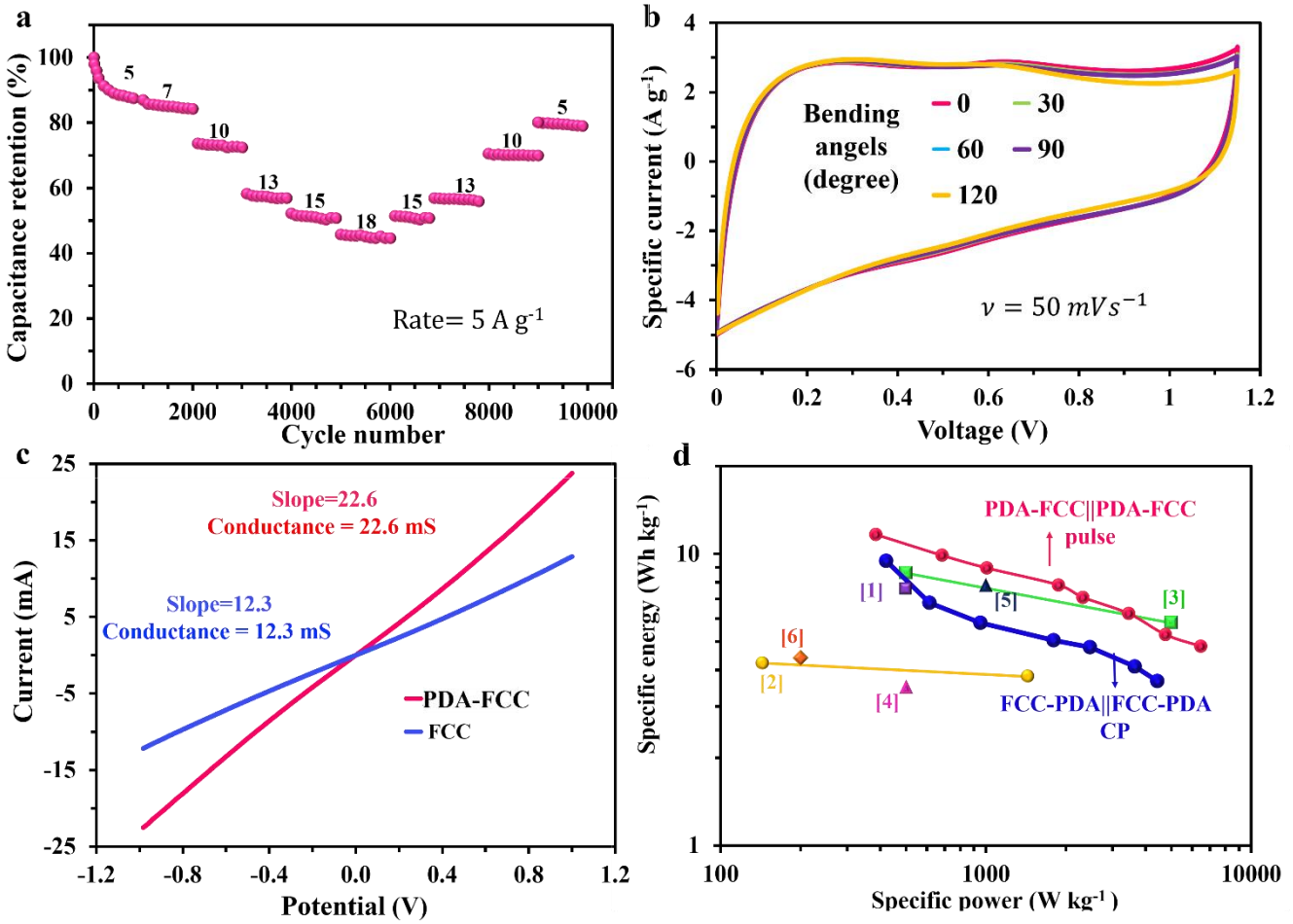

Fig. 5 Evaluation of cycling stability, and flexibility of the PDA-FCC||PDA-FCC device along with a Ragone plot. (a) Cycle life performance of the PDA-FCC||PDA-FCC device at different specific current values from 5.0 to 18.0 A g^{-1} in a PVA-in-H_2SO_4 gel electrolyte. (b) CV curves (υ = 50 mV s^{-1}) of the PDA-FCC||PDA-FCC device (1.0 cm × 1.0 cm) at different bending angles from 0° to 120°. The bending radii of curvature at bending angles of 30, 60, 90, and 120º are 4.7, 4.3, 3.5, and 2.5 mm, respectively. (c) Solid state conductivity studies of the materials. I–V plots of the FCC and PDA-FCC electrodes in an electrolyte-free medium. (d) Ragone plot of PDA-FCC||PDA-FCC device and its comparison with some reported similar devices. [1] C-PDA/PMA,[67] [2] rGO/CNTNH2/PDA,[92] [3] PpPD/graphene,[93][4] C-PDA,[60] [5] SPAN-FC[94] and [6] CFC/PEDOT[26]

Figure 4b displays CV curves of the symmetric pulse-deposited PDA-FCC||PDA-FCC device at different voltage ranges from 0.9 to 1.25 V in a PVA-in-H_2SO_4 (1.0 M) gel electrolyte. The device can endure a voltage window of 1.3 V based on the CV curve of the PDA-FCC electrode in a three-electrode cell setup (in a 1.0 M H_2SO_4 electrolyte). However, to sustain a long-term stability for the all-solid-state symmetric device, we slightly shrunk the operating voltage window to suppress potential cycling-induced structural pulverization or overoxidation/overreduction of the polydopamine film and recorded CV curves of the device in the voltages range of 1.2 V.

Figure 4c shows CV curves of the pulse-deposited PDA-FCC||PDA-FCC device at different scan rates from 5 to 600 mV s^{-1}, and those of the CP-deposited PDA-FCC||PDA-FCC device (in the range from 5 to 400 mV s^{-1}) and FCC||FCC device (in the range from 10 to 400 mV s^{-1}) are presented in Fig. S13 and Fig. S14, respectively. As can be seen, the CV curves of the pulse-deposited PDA-FCC||PDA-FCC supercapacitors retain their pseudo-rectangular shape even at a high scan rate of 600 mV s^{-1}; whereas the CV curves of the FCC||FCC supercapacitor significantly deviates from a rectangular shape and becomes very resistive when the scan rate exceeds 300 mV s^{-1}. This Simplies a better rate capability and a faster charge-discharge kinetics for the PDA-FCC||PDA-FCC device.

GCD profiles of the pulse-deposited PDA-FCC||PDA-FCC device at various specific current values from 1.0 to 18.0 A g^{-1}, areal current densities from 2.0 to 20.0 mA cm^{-2}, and volumetric current densities from 5.0 to 60.0 mA cm^{-3} are provided in Fig. 4d-f, respectively. A negligible *iR* drop at the start of all discharge profiles indicates a fast charge and ion transport in the device. GCD profiles of the CP-deposited PDA-FCC||PDA-FCC device are presented in Fig.s S15-S17.

Figure 4g-i shows rate capability studies of the CP- and pulse-deposited PDA-FCC||PDA-FCC devices. As depicted in Fig. 4, the pulse deposited PDA-FCC||PDA-FCC device displays an excellent specific capacitance of 61 F g^{-1} at 1.0 A g^{-1} (24 F g^{-1} at 0.5 A g^{-1} based on the total mass of the electrode, Fig. 4g), areal capacitance of 195 mF cm^{-2} at 1.6 mA cm^{-2} (Fig. 4h), and volumetric capacitance of 325 mF cm^{-3} at 5.3 mA cm^{-3} (Fig. 4i) and retains specific capacitance of 24 F g^{-1} at 18.0 A g^{-1}, areal capacitance of 77 mF cm^{-2} at 28.8 mA cm^{-2}, and volumetric capacitance of 128 mF cm^{-3} at 96.0 mA cm^{-3} (40 % capacitance

retention), further revealing the excellent rate capability of the pulse-deposited PDA-FCC||PDA-FCC device in comparison with other polymer-based symmetric devices (Table S5).

The long-term cycling stability of a device is an essential requirement to meet practical applicability. We investigated cycling stability of a pulse-deposited PDA-FCC||PDA-FCC device by recording 10,000 GCD cycles at different specific currents from 5.0 to 18.0 and then back to 5 A g^{-1} (1,000 cycles at each rate). The device lost almost 10% of its initial capacitance over the first 1,000 cycles at a specific current of 5.0 A g^{-1} and the capacitance decreased very slowly thereafter so that the device retained about 80% of the initial specific capacitance after 10,000 cycles at different rates (Fig. 5a), implying good durability and electrochemical performance for the symmetric PDA-FCC||PDA-FCC device. The improved cycling stability demonstrates strong interactions between catechol and amine moieties of the PDA with oxygen-containing functional groups of the FCC. Note that by extending the operating voltage window of the symmetric PDA-FCC||PDA-FCC device to 1.3 V, the device retains 65% of the initial capacitance after 10,000 cycles (via the same steps displayed in Fig. 5a). Chemical degradation, which is mainly the consequence of over-oxidation or over-reduction of the electrode active materials, is a possible degradation pathway for the PDA-FCC during the long-term GCD cycling. The CP and pulse-deposited PDA-FCC||PDA-FCC devices retain 74% and 75% of their initial capacitance by recording 10,000 consecutive GCD cycles at a specific current of 5.0 A g^{-1} (Fig. S18, Supporting Information).

Mechanical deformation of the as-fabricated device was evaluated under various bending states. As shown in Fig. 5b, the CV curves of the device displays a negligible change at different bending angles (from 30° to 120° corresponding to radii of curvature from 4.7 to 2.5 mm, respectively), indicating the robustness and mechanical flexibility of the device. The satisfactory performance under mechanical bending is due to strong immobilization of polydopamine on the flexible FCC substrate.

For conductivity measurements, we plotted the I-E graph for the FCC and PDA-FCC in the solid state that shows conductance values of 12.3 and 22.6 mS for the FCC and PDA-FCC, respectively, (Fig. 5c). The enhanced conductivity of the PDA-FCC electrode can be attributed to the diminution of the HOMO-LUMO gap from 4.14 eV to 3.18 eV after polymerization of dopamine molecules into polydopamine.[91]

Specific energy and specific power of the prepared PDA-FCC||PDA-FCC device, as two of the fundamental parameters for the characterization of energy storage devices, are presented in a Ragone plot (Fig. 5d). The device provides a specific energy of up to 11.7 W h kg^{-1} at a specific power of 385.3 W kg^{-1} and a volumetric energy density of up to 38.1 W h cm^{-3} at a volumetric power density of 2,131.0 W cm^{-3} and can still maintain a specific energy of 4.7 W h kg^{-1} at a high specific power of 6,400.0 W kg^{-1} and a volumetric energy density of 28.9 W h cm^{-3} at a volumetric power density of 22,000.0 W cm^{-3}. These values reveal the excellent energy/power performance of the as-fabricated PDA-FCC||PDA-FCC device, which are higher than or comparable to those of the previously reported metal-free symmetric devices (Table S5).[26, 60, 92]

In order to evaluate the potential of the symmetric PDA-FCC||PDA-FCC device for practical applications in real energy-storage systems, we connected two as-fabricated devices in series and fully charged the assembly at 2.2 V. The assembled devices light a red LED (1.8 V, 20 mA) for more than 6 min and can turn on a mini-motor (1.0 V, 30 mW) for several seconds (Video S2, and S3). The excellent practical applicability of the symmetric PDA-FCC||PDA-FCC device suggests its potential, as a flexible solid-state metal-free supercapacitor, for state-of-the-art applications.

According to the EIS measurements of the symmetric PDA-FCC||PDA-FCC device at an open-circuit voltage over the frequency range from 100 kHz to 10 mHz (Fig. S19), a Nyquist plot of the device consists of a semicircle at high frequency followed by a near-vertical line at low frequency, with an ESR of 2.1 Ω and a small R_{ct} of 0.7 Ω, indicating the good conductivity and fast reaction kinetics of the electrode materials. More detailed interpretations of the Bode plots can be found in the Supporting Information (Fig. S19).

Conclusions

In summary, we have employed two novel, facile and convenient one-pot electro-synthetic procedures (constant potential and pulsed potential deposition techniques) for the electro-deposition of polydopamine on a flexible functionalized carbon cloth (FCC) substrate to prepare a pseudocapacitive electrode material that does not need any post-preparation process. Excellent pseudocapacitive behavior of the pulse-deposited PDA-FCC electrode along with its wide operating potential window can be ascribed to the effective conjugation between catechol and amine moieties of PDA and the oxygen-bearing functional groups of the FCC. Promising and desirable electrochemical characteristics of the PDA-FCC electrode that outperforms most polymer-based active materials reveals suitability of our designed electrode for more sustainable development. The symmetric solid-state PDA-FCC||PDA-FCC device (prepared *via* the pulse deposition approach) delivers a high specific energy of 11.7 W h kg^{-1}, an excellent specific power of 6.4 kW kg^{-1}, along with an outstanding cycling stability over 10,000 consecutive GCD cycles, and excellent flexibility, demonstrating that our device design is a promising approach for the development of high-performance metal-free green supercapacitors.

Author Contributions

Masumeh Moloudi: Conceptualization, Data curation, Formal analysis, Writing - original draft. **Mohammad S. Rahmanifar**: Conceptualization, Writing review & editing, Validation. **Abolhassan Noori**: Conceptualization, Writing review & editing, Validation. **Xueying Chang**: Formal analysis. **Richard B. Kaner**: Supervision, Validation, Writing review & editing, Resources.

Mir F. Mousavi: Supervision, Conceptualization, Validation, Writing - review & editing, Resources.

Conflicts of interest

There are no conflicts to declare.

Acknowledgements

This work was made possible through financial support from Tarbiat Modares University Research Council, Iranian National Science Foundation, INSF, grant number 98013363, as well as the Research Core of Tarbiat Modares University, grant number IG-39802 (M.F.M) and the Dr. Myung Ki Hong Endowed Chair in Materials Innovation at UCLA (R.B.K).

Notes and references

1. W.-J. Liu, H. Jiang and H.-Q. Yu, *Energy Environ. Sci.*, 2019, **12**, 1751-1779.
2. T. Liu, L. Zhang, B. Cheng and J. Yu, *Adv. Energy Mater.*, 2019, **9**, 1803900.
3. H. Jin, J. Li, Y. Yuan, J. Wang, J. Lu and S. Wang, *Adv. Energy Mater.*, 2018, **8**, 1801007.
4. V. C. Broto and J. Kirshner, *Nat. Energy*, 2020, **5**, 419-421.
5. A. Hollas, X. Wei, V. Murugesan, Z. Nie, B. Li, D. Reed, J. Liu, V. Sprenkle and W. Wang, *Nat. Energy*, 2018, **3**, 508-514.
6. L. J. Wang, M. F. El‐Kady, S. Dubin, J. Y. Hwang, Y. Shao, K. Marsh, B. McVerry, M. D. Kowal, M. F. Mousavi and R. B. Kaner, *Adv. Energy Mater.*, 2015, **5**, 1500786.
7. H. Shao, Y.-C. Wu, Z. Lin, P.-L. Taberna and P. Simon, *Chem. Soc. Rev.*, 2020, **49**, 3005-3039.
8. M. R. Lukatskaya, S. Kota, Z. Lin, M.-Q. Zhao, N. Shpigel, M. D. Levi, J. Halim, P.-L. Taberna, M. W. Barsoum and P. Simon, *Nat. Energy*, 2017, **2**, 17105.
9. Y. Shao, M. F. El-Kady, L. J. Wang, Q. Zhang, Y. Li, H. Wang, M. F. Mousavi and R. B. Kaner, *Chem. Soc. Rev.*, 2015, **44**, 3639-3665.
10. M. Ghidiu, M. R. Lukatskaya, M.-Q. Zhao, Y. Gogotsi and M. W. Barsoum, *Nature*, 2014, **516**, 78-81.
11. H. Ji, X. Zhao, Z. Qiao, J. Jung, Y. Zhu, Y. Lu, L. L. Zhang, A. H. MacDonald and R. S. Ruoff, *Nat. Commun.*, 2014, **5**, 1-7.
12. M. F. El-Kady, V. Strong, S. Dubin and R. B. Kaner, *Science*, 2012, **335**, 1326-1330.
13. R. Hou, B. Liu, Y. Sun, L. Liu, J. Meng, M. D. Levi, H. Ji and X. Yan, *Nano Energy*, 2020, **72**, 104728.
14. C. Wang, V. Strauss and R. B. Kaner, *Trends Chem.*, 2019, **1**, 858-868.
15. M. S. Rahmanifar, M. Hemmati, A. Noori, M. F. El-Kady, M. F. Mousavi and R. B. Kaner, *Mater. Today Energy*, 2019, **12**, 26-36.
16. Q. Yun, L. Li, Z. Hu, Q. Lu, B. Chen and H. Zhang, *Adv. Mater.*, 2020, **32**, 1903826.
17. A. Pendashteh, M. S. Rahmanifar, R. B. Kaner and M. F. Mousavi, *Chem. Commun.*, 2014, **50**, 1972-1975.
18. L. Lin, W. Lei, S. Zhang, Y. Liu, G. G. Wallace and J. Chen, *Energy Storage Mater.*, 2019, **19**, 408-423.
19. J. Ma, X. Guo, Y. Yan, H. Xue and H. Pang, *Adv. Sci.*, 2018, **5**, 1700986.
20. A. Pendashteh, M. F. Mousavi and M. S. Rahmanifar, *Electrochim. Acta*, 2013, **88**, 347-357.
21. P. Geng, S. Zheng, H. Tang, R. Zhu, L. Zhang, S. Cao, H. Xue and H. Pang, *Adv. Energy Mater.*, 2018, **8**, 1703259.
22. M. Hashemi, M. S. Rahmanifar, M. F. El-Kady, A. Noori, M. F. Mousavi and R. B. Kaner, *Nano Energy*, 2018, **44**, 489-498.
23. C. Zhao, X. Jia, K. Shu, C. Yu, G. G. Wallace and C. Wang, *J. Mater. Chem. A*, 2020, **8**, 4677-4699.
24. Z. Wang, M. Zhu, Z. Pei, Q. Xue, H. Li, Y. Huang and C. Zhi, *Mater. Sci. Eng., R*, 2020, **139**, 100520.
25. M. F. Mousavi, M. Hashemi, M. S. Rahmanifar and A. Noori, *Electrochim. Acta*, 2017, **228**, 290-298.
26. M. Rajesh, C. J. Raj, R. Manikandan, B. C. Kim, S. Y. Park and K. H. Yu, *Mater. Today Energy*, 2017, **6**, 96-104.
27. Z. Li, G. Ma, R. Ge, F. Qin, X. Dong, W. Meng, T. Liu, J. Tong, F. Jiang and Y. Zhou, *Angew. Chem. Int. Ed.*, 2016, **55**, 979-982.
28. H. R. Ghenaatian, M. F. Mousavi and M. S. Rahmanifar, *Synth. Met.*, 2011, **161**, 2017-2023.
29. M. Boota, B. Anasori, C. Voigt, M. Q. Zhao, M. W. Barsoum and Y. Gogotsi, *Adv. Mater.*, 2016, **28**, 1517-1522.
30. C. C. Hou and Q. Xu, *Adv. Energy Mater.*, 2019, **9**, 1801307.
31. M. S. Rahmanifar, H. Hesari, A. Noori, M. Y. Masoomi, A. Morsali and M. F. Mousavi, *Electrochim. Acta*, 2018, **275**, 76-86.
32. S. Bi, H. Banda, M. Chen, L. Niu, M. Chen, T. Wu, J. Wang, R. Wang, J. Feng and T. Chen, *Nat. Mater.*, 2020, **19**, 552-558.
33. D. Sheberla, J. C. Bachman, J. S. Elias, C.-J. Sun, Y. Shao-Horn and M. Dincă, *Nat. Mater.*, 2017, **16**, 220.
34. Y. Shabangoli, M. F. El‐Kady, M. Nazari, E. Dadashpour, A. Noori, M. S. Rahmanifar, X. Lv, C. Zhang, R. B. Kaner and M. F. Mousavi, *Small*, 2020, **16**, 2001340.
35. A.-L. Yan, X.-C. Wang and J.-P. Cheng, *Nanomaterials*, 2018, **8**, 747.
36. H. J. Nam, E. B. Park and D.-Y. Jung, *RSC Adv.*, 2016, **6**, 24952-24958.
37. Y. Shabangoli, M. S. Rahmanifar, M. F. El-Kady, A. Noori, M. F. Mousavi and R. B. Kaner, *Energy Storage Mater.*, 2018, **11**, 282-293.
38. Z. Lin, H. Shao, K. Xu, P.-L. Taberna and P. Simon, *Trends Chem.*, 2020, **2**, 654-664.
39. J. Pang, R. G. Mendes, A. Bachmatiuk, L. Zhao, H. Q. Ta, T. Gemming, H. Liu, Z. Liu and M. H. Rummeli, *Chem. Soc. Rev.*, 2019, **48**, 72-133.
40. J. Yang, W. Bao, P. Jaumaux, S. Zhang, C. Wang and G. Wang, *Adv. Mater. Interfaces*, 2019, **6**, 1802004.
41. Y. Shabangoli, M. S. Rahmanifar, A. Noori, M. F. El-Kady, R. B. Kaner and M. F. Mousavi, *ACS Nano*, 2019, **13**, 12567-12576.
42. Y. Shabangoli, M. S. Rahmanifar, M. F. El-Kady, A. Noori, M. F. Mousavi and R. B. Kaner, *Adv. Energy Mater.*, 2018, **8**, 1802869.
43. S. Gong, H. Ni, L. Jiang and Q. Cheng, *Mater. Today*, 2017, **20**, 210-219.
44. C. Gong, S. Sun, Y. Zhang, L. Sun, Z. Su, A. Wu and G. Wei, *Nanoscale*, 2019, **11**, 4147-4182.
45. H. Zhang, X. He, F. Wei, S. Dong, N. Xiao and J. Qiu, *ACS Sustainable Chem. Eng.*, 2020, **8**, 3065-3071.
46. J. Lian, D. Pang, C. Yang, L. Xiong, R. Cheng, S. Yang, J. Lei, T. Chen, F. Yang and W. Zhu, *New J. Chem.*, 2020, **44**, 1400-1406.
47. C. Wu, T. Zhou, Y. Du, S. Dou, H. Zhang, L. Jiang and Q. Cheng, *Nano Energy*, 2019, **58**, 517-527.
48. C. Huang, L. Kang, N. Zhang, S. Wan, X. Zhou and J. Zhang, *ACS Appl. Mater. Interfaces*, 2019, **11**, 38303-38312.
49. L. Peng, Y. Cai, Y. Luo, G. Yuan, J. Huang, C. Hu, H. Dong, Y. Xiao, Y. Liang and Y. Liu, *ACS Sustainable Chem. Eng.*, 2018, **6**, 12716-12726.

50. X. Geng, Y. Zhang, L. Jiao, L. Yang, J. Hamel, N. Giummarella, G. Henriksson, L. Zhang and H. Zhu, *ACS Sustainable Chem. Eng.*, 2017, **5**, 3553-3561.
51. B. Li, R. Xing, S. V. Mohite, S. S. Latthe, A. Fujishima, S. Liu and Y. Zhou, *J. Power Sources*, 2019, **436**, 226862.
52. Q. N. Wu, J. H. Wen, M. Wen, Q. S. Wu and Y. Q. Fu, *J. Mater. Chem. A*, 2018, **6**, 15781-15788.
53. K. Song, X. Wang, J. Wang, B. Zhang and C. Zuo, *ChemElectroChem*, 2018, **5**, 1297-1305.
54. Y. Liu, K. Ai and L. Lu, *Chem. Rev.*, 2014, **114**, 5057-5115.
55. H. Lee, B. P. Lee and P. B. Messersmith, *Nature*, 2007, **448**, 338-341.
56. H. Lee, S. M. Dellatore, W. M. Miller and P. B. Messersmith, *Science*, 2007, **318**, 426-430.
57. Q. Huang, J. Chen, M. Liu, H. Huang, X. Zhang and Y. Wei, *Chem. Eng. J.*, 2020, 124019.
58. S. El Yakhlifi and V. Ball, *Colloids Surf., B*, 2020, **186**, 110719.
59. K. Qu, Y. Wang, A. Vasileff, Y. Jiao, H. Chen and Y. Zheng, *J. Mater. Chem. A*, 2018, **6**, 21827-21846.
60. Z. J. Zhang, G. L. Deng, X. Huang, X. Wang, J. M. Xue and X. Y. Chen, *Electrochim. Acta*, 2020, **339**, 135940.
61. Z. Miao, Y. Huang, J. Xin, X. Su, Y. Sang, H. Liu and J.-J. Wang, *ACS Appl. Mater. Interfaces*, 2019, **11**, 18044-18050.
62. Z. Tabti, R. Ruiz-Rosas, C. s. Quijada, D. Cazorla-Amorós and E. Morallon, *ACS Appl. Mater. Interfaces*, 2014, **6**, 11682-11691.
63. G. Wang, H. Wang, X. Lu, Y. Ling, M. Yu, T. Zhai, Y. Tong and Y. Li, *Adv. Mater.*, 2014, **26**, 2676-2682.
64. S. Jiang, T. Shi, X. Zhan, H. Long, S. Xi, H. Hu and Z. Tang, *J. Power Sources*, 2014, **272**, 16-23.
65. Y. Ding, M. Floren and W. Tan, *Biosurf. Biotribol.*, 2016, **2**, 121-136.
66. A. Noori, M. F. El-Kady, M. S. Rahmanifar, R. B. Kaner and M. F. Mousavi, *Chem. Soc. Rev.*, 2019, **48**, 1272-1341.
67. X. Chen, Q. Z. Song, W. X. He, P. P. Liu, Y. H. Xiao and J. Y. Liang, *Dalton Transact.*, 2019, **48**, 17321-17330.
68. N. Holten-Andersen, M. J. Harrington, H. Birkedal, B. P. Lee, P. B. Messersmith, K. Y. C. Lee and J. H. Waite, *Proc. Natl. Acad. Sci.*, 2011, **108**, 2651-2655.
69. Y. Liu, Z. Liu, Y. Liu, H. Hu, Y. Li, P. Yan, B. Yu and F. Zhou, *Small*, 2015, **11**, 426-431.
70. K. Kordek, L. Jiang, K. Fan, Z. Zhu, L. Xu, M. AlMamun, Y. Dou, S. Chen, P. Liu and H. Yin, *Adv. Energy Mater.*, 2018, 1802936.
71. W. Lee, J. U. Lee, B. M. Jung, J.-H. Byun, J.-W. Yi, S.-B. Lee and B.-S. Kim, *Carbon*, 2013, **65**, 296-304.
72. J. Tan, Z. Zhang, Y. He, Q. Yue, Z. Xie, H. Ji, Y. Sun, W. Shi and D. Ge, *Synth. Met.*, 2017, **234**, 86-94.
73. P. Vecera, J. C. Chacón-Torres, T. Pichler, S. Reich, H. R. Soni, A. Görling, K. Edelthalhammer, H. Peterlik, F. Hauke and A. Hirsch, *Nat. Commun.*, 2017, **8**, 1-9.
74. M. T. Cortés, C. Vargas, D. A. Blanco, I. D. Quinchanegua, C. Cortés and A. M. Jaramillo, *J. Chem. Educ.*, 2019, **96**, 1250–1255.
75. T. Liu, B. Lee, B. G. Kim, M. J. Lee, J. Park and S. W. Lee, *Small*, 2018, **14**, 1801236.
76. T. Xiong, W. S. V. Lee, L. Chen, T. L. Tan, X. Huang and J. Xue, *Energy Environ. Sci.*, 2017, **10**, 2441-2449.
77. R. A. Zangmeister, T. A. Morris and M. J. Tarlov, *Langmuir*, 2013, **29**, 8619-8628.
78. Y. Wang, B. Chen, Y. Zhang, L. Fu, Y. Zhu, L. Zhang and Y. Wu, *Electrochim. Acta*, 2016, **213**, 260-269.
79. L. Qie, W. Chen, H. Xu, X. Xiong, Y. Jiang, F. Zou, X. Hu, Y. Xin, Z. Zhang and Y. Huang, *Energy Environ. Sci.*, 2013, **6**, 2497-2504.
80. Y. Y. Smolin, K. L. Van Aken, M. Boota, M. Soroush, Y. Gogotsi and K. K. Lau, *Adv. Mater. Interfaces*, 2017, **4**, 1601201.
81. W. He, C. Wang, F. Zhuge, X. Deng, X. Xu and T. Zhai, *Nano Energy*, 2017, **35**, 242-250.
82. H. Coskun, A. Aljabour, P. d. Luna, H. Sun, N. Nishiumi, T. Yoshida, G. Koller, M. G. Ramsey, T.Greunz, D. Stifter, M. Strobel, S. Hild, A. W. Hassel, N. S. Sariciftci, E. H. Sargent and P. Stadler, *Adv. Mater.* 2020, ***32***, 1902177.
83. A. Galal, N. F. Atta and S. M. Ali, *Appl. Catal., A*, 2011, **409**, 202-208.
84. D. Qu, G. Wang, J. Kafle, J. Harris, L. Crain, Z. Jin and D. Zheng, *Small Methods*, 2018, **2**, 1700342.
85. B.-A. Mei, O. Munteshari, J. Lau, B. Dunn and L. Pilon, *J. Phys. Chem. C*, 2018, **122**, 194-206.
86. B.-A. Mei, J. Lau, T. Lin, S. H. Tolbert, B. S. Dunn and L. Pilon, *J. Phys. Chem. C*, 2018, **122**, 24499-24511.
87. R. Thangappan, S. Kalaiselvam, A. Elayaperumal, R. Jayavel, M. Arivanandhan, R. Karthikeyan and Y. Hayakawa, *Dalton Transact.*, 2016, **45**, 2637-2646.
88. A. Lasia, in *Modeling and Numerical Simulations*, Springer, 2008, pp. 67-137.
89. C. Wang, A. J. Appleby and F. E. Little, *J. Electrochem. Soc.*, 2003, **150**, A143-A148.
90. T. S. Mathis, N. Kurra, X. Wang, D. Pinto, P. Simon and Y. Gogotsi, *Adv. Energy Mater.*, 2019, **9**, 1902007.
91. B. S. Yin, S. W. Zhang, K. Ke and Z.-B. Wang, *Chem. Eng. J.*, 2019, **375**, 122056.
92. R. Zeng, H. Deng, Y. Xiao, J. Huang, K. Yuan and Y. Chen, *Compos. Commun.*, 2018, **10**, 73-80.
93. S. Ramaprabhu, *J. Mater. Chem.*, 2012, **22**, 18775-18783.
94. L. J. Bian, F. Luan, S. S. Liu and X. X. Liu, *Electrochim. Acta*, 2012, **64**, 17-22.